Topologically nontrivial configurations associated with Hopf charges investigated in the two-component Ginzburg-Landau model

Juha Jäykkä* and Jarmo Hietarinta†
Department of Physics, University of Turku, FI-20014 Turku, Finland

Petri Salo‡
Laboratory of Physics, Helsinki University of Technology, P.O. Box 1100, FI-02015 TKK, Espoo, Finland
(Received 21 August 2006; revised manuscript received 7 November 2007; published 10 March 2008)

We study the stability of Hopfions embedded in the Ginzburg-Landau (GL) model of two oppositely charged components. It has been shown by Babaev *et al.* [Phys. Rev. B **65**, 100512 (2002)] that this model contains the Faddeev-Skyrme (FS) model, which is known to have topologically stable configurations with a given Hopf charge, the so-called Hopfions. Hopfions are typically formed from a unit-vector field that points to a fixed direction at spatial infinity and locally forms a knot with a soft core. The GL model, however, contains extra fields beyond the unit-vector field of the FS model and this can, in principle, change the fate of topologically nontrivial configurations. We investigate the stability of Hopfions in the two-component GL model both analytically (scaling) and numerically (first order dissipative dynamics). A number of initial states with different Hopf charges are studied; we also consider various different scalar potentials, including a singular one. In all the cases studied, we find that the Hopfions tend to shrink into a thin loop that is too close to a singular configuration for our numerical methods to investigate.

DOI: 10.1103/PhysRevB.77.094509 PACS number(s): 74.20.De, 47.32.cd

I. INTRODUCTION

Topologically stable knots and other vortexlike structures have recently received wide interest within condensed matter physics. One reason for this is the continuous development of experimental techniques which now allow the production of vortices in various types of media. These include, e.g., the Bose-Einstein condensates,[1,2] superconductors,[3–5] superfluid ^{3}He,[6,7] and nematic liquid crystals.[8] At the same time, the increased capacity of supercomputers has made it possible to study these structures numerically. Thus, in the last decade, there have been many numerical studies devoted to finding stable topologically nontrivial configurations in different physical systems, including, e.g., topological unknots, knots and vortices in the Faddeev-Skyrme (FS) model,[9–15] vortices in the Bose-Einstein condensates,[16–18] vortex atom lasers in a two-flavor Bose condensate,[19] and vortices in superconductors,[20,21] liquid helium,[22,23] liquid metallic hydrogen,[24] and possibly even in neutron stars.[25]

There are various ways in which a vector field in nature can support vortices. For example, a velocity field can form a vortex, e.g., in a hurricane. The position of the vortex is in the eye of the hurricane, where the velocity is zero. Such a vortex is not stable because a velocity field can continuously change to zero everywhere.

In some special materials, there can exist vector fields, associated with spin or other such property, which cannot vanish. Then, it is possible to have vortices that are both nonsingular and conserved, the conservation following from topological reasons. (One example that can be produced in a laboratory is the continuous unlocked vortex in superfluid ^{3}He-*A*.[6]) The prototype model that contains nonvanishing topological structures characterized by a Hopf charge was presented by Faddeev,[26] and recently it has been shown numerically that this model does indeed contain stable topological solitons.[10–13]

In this work, we study numerically a system of two electromagnetically coupled, oppositely charged Bose condensates described by the Ginzburg-Landau (GL) model. Babaev *et al.* studied this system in Ref. 27 and argued that it should contain stable knotted vortex solitons with a nonzero Hopf charge. Here, we present our results for the GL model, the main conclusion being that Hopfions in the GL model do not exhibit the same kind of stability as in the FS model.

The paper is organized as follows. In Sec. II, we formulate the equations, discuss the possible potentials, and present the initial states that are used in the computation. In Sec. III, we present the discretization of the GL Lagrangian and the numerical method for finding stable minimum energy configurations. In Sec. IV, we describe the results, and finally, in Sec. V, we give some concluding remarks on the results obtained.

II. MODEL

A. Ginzburg-Landau model

The model describes two electromagnetically coupled, oppositely charged Bose condensates, as given by the GL Lagrangian density,

$$\mathcal{L} = \frac{\hbar^2}{2m_1}\left|\left(\nabla + i\frac{2e}{\hbar c}\vec{A}\right)\Psi_1\right|^2 + \frac{\hbar^2}{2m_2}\left|\left(\nabla - i\frac{2e}{\hbar c}\vec{A}\right)\Psi_2\right|^2 + V(\Psi_1,\Psi_2) + \frac{1}{2\mu_0}\vec{B}^2, \tag{1}$$

where we have used SI units. In Eq. (1), Ψ_1 and Ψ_2 are the order parameters for the condensates, $\vec{A}$ is the electromagnetic vector potential, $\vec{B}$ the magnetic field, $\vec{B}=\frac{1}{c}\nabla\times\vec{A}$, and V is a potential.

Babaev *et al.*[27] introduced new variables by setting

$$\Psi_\alpha = \sqrt{2m_\alpha}\rho\chi_\alpha, \tag{2}$$

where the new complex field χ is normalized as

$$|\chi_1|^2 + |\chi_2|^2 = 1, \tag{3}$$

and therefore the real field ρ is given by

$$\rho^2 = \frac{1}{2}\left(\frac{|\Psi_1|^2}{m_1} + \frac{|\Psi_2|^2}{m_2}\right). \tag{4}$$

In terms of the new fields of Eq. (2), Eq. (1) becomes

$$\mathcal{L} = \hbar^2\rho^2\left[\left|\left(\nabla + i\frac{2e}{\hbar c}\vec{A}\right)\chi_1\right|^2 + \left|\left(\nabla - i\frac{2e}{\hbar c}\vec{A}\right)\chi_2\right|^2\right] + \hbar^2(\nabla\rho)^2 + V(\chi_1,\chi_2,\rho^2) + \frac{1}{2\mu_0}\vec{B}^2. \tag{5}$$

The Lagrangian (1) is invariant under the gauge transformation,

$$\begin{cases} \Psi_1 \to e^{-i\frac{2e}{\hbar}\theta(x)}\Psi_1, \\ \Psi_2 \to e^{i\frac{2e}{\hbar}\theta(x)}\Psi_2, \\ A_\mu \to A_\mu + c\partial_\mu\theta(x), \end{cases} \tag{6}$$

and the corresponding Noether current is

$$J_k := \frac{i\hbar e}{m_1}(\Psi_1^*\partial_k\Psi_1 - \Psi_1\partial_k\Psi_1^*) - \frac{i\hbar e}{m_2}(\Psi_2^*\partial_k\Psi_2 - \Psi_2\partial_k\Psi_2^*) - \frac{4e^2}{c}\left(\frac{|\Psi_1|^2}{m_1} + \frac{|\Psi_2|^2}{m_2}\right)A_k, \tag{7}$$

which, using Ampère's law, must satisfy

$$\vec{J} = \nabla \times \vec{B} = \frac{1}{c}\nabla \times \nabla \times \vec{A}. \tag{8}$$

When we use the new variables [Eq. (2)] here, we obtain

$$J_k = 2e\hbar\rho^2 i(\chi_1^*\partial_k\chi_1 - \chi_1\partial_k\chi_1^* - \chi_2^*\partial_k\chi_2 + \chi_2\partial_k\chi_2^*) - \frac{8e^2\rho^2}{c}A_k = 4e\hbar\rho^2\left(\tfrac{1}{2}j_k - \frac{2e}{\hbar c}A_k\right), \tag{9}$$

which contains a new (nongauge invariant) current,[28]

$$j_k = i(\chi_1^*\partial_k\chi_1 - \chi_1\partial_k\chi_1^* - \chi_2^*\partial_k\chi_2 + \chi_2\partial_k\chi_2^*). \tag{10}$$

Later on, we also use a gauge invariant vector field,

$$\vec{C} := \frac{1}{\hbar e\rho^2}\vec{J}. \tag{11}$$

Next, we define the unit vector field $\vec{n}$ by

$$\vec{n} = (\chi_1^* \ \chi_2)\vec{\sigma}\begin{pmatrix}\chi_1 \\ \chi_2^*\end{pmatrix} = \begin{pmatrix}\chi_1\chi_2 + \chi_1^*\chi_2^* \\ i(\chi_1\chi_2 - \chi_1^*\chi_2^*) \\ |\chi_1|^2 - |\chi_2|^2\end{pmatrix}, \tag{12}$$

where $\vec{\sigma}$ are the Pauli matrices. The inverse transformation is

$$\begin{cases} \chi_1 = \dfrac{n_1 - in_2}{\sqrt{2(1-n_3)}}e^{i\alpha}, \\ \chi_2 = \dfrac{\sqrt{(1-n_3)}}{\sqrt{2}}e^{-i\alpha}, \end{cases} \tag{13}$$

where the phase must be chosen so that χ_α are continuous, see, e.g., Eq. (33). (This inverse transformation is not used in the numerical simulations.)

In order to show the similarities between the GL and FS models, we write the Lagrangian (5) in terms of $\vec{n}$, ρ, and $\vec{C}$, after which the $\vec{n}$ part of the result should be similar to the FS model, given by

$$\mathcal{L}_{FS} = \tfrac{1}{2}\partial_k n_l\partial^k n^l + g_{FS}(\vec{n}\cdot\partial_k\vec{n}\times\partial_l\vec{n})^2. \tag{14}$$

After inverting Eqs. (9) and (11) to obtain $\vec{A}$ in terms of $\vec{C}$ and $\vec{j}$, the kinetic part of Eq. (5) becomes

$$\mathcal{L}_{\text{kinetic}} = \hbar^2\rho^2\left(|\nabla\chi_1|^2 + |\nabla\chi_2|^2 - \tfrac{1}{4}\vec{j}^2\right) + \hbar^2(\nabla\rho)^2 + \frac{\hbar^2\rho^2}{16}\vec{C}^2. \tag{15}$$

Using Eqs. (12), (3), and (10), one finds that

$$\partial_k n_l\partial^k n^l = 4(|\nabla\chi_1|^2 + |\nabla\chi_2|^2) - \vec{j}^2, \tag{16}$$

and therefore the first term in Eq. (15) corresponds to the first term in Eq. (14).

By direct substitution of Eqs. (9) and (11) into $\vec{B}$, we also find that

$$\vec{B} = \frac{1}{c}\nabla \times \vec{A} = \frac{\hbar}{4e}\left(\nabla \times \vec{j} - \tfrac{1}{2}\nabla \times \vec{C}\right), \tag{17}$$

and again using Eqs. (12), (3), and (10), we get

$$\tfrac{1}{2}\epsilon_{klm}\vec{n}\cdot\partial_l\vec{n}\times\partial_m\vec{n} = -\epsilon_{klm}\partial_l j_m, \tag{18}$$

from which we can see that the $\vec{B}^2$ term in Eq. (5) contributes to the second term in Eq. (14).

Combining the above results, we can write the Lagrangian (1) in the form

$$\mathcal{L} = \frac{\hbar^2\rho^2}{4}\partial_k n_l\partial^k n^l + \hbar^2(\nabla\rho)^2 + \frac{\hbar^2\rho^2}{16}\vec{C}^2 + V(\rho,n_k) + \frac{\hbar^2}{128\mu_0 e^2}[\epsilon_{klm}(\vec{n}\cdot\partial_k\vec{n}\times\partial_l\vec{n} + \partial_k C_l)]^2, \tag{19}$$

which is the form derived by Babaev *et al.*[27] The dynamical fields are now ρ, $\vec{n}$, and $\vec{C}$. If ρ=constant and $\vec{C}$=0, the GL model reduces to the FS model in Eq. (14). Since the FS model contains stable topological structures with nontrivial Hopf charge, one can hope that the GL model also contains similar structures. However, GL contains the additional fields ρ and $\vec{C}$ in comparison to FS and the role of these new fields must be investigated.

B. Form of the potential

A typical and rather general quartic potential used in the GL model is

$$V_0(\Psi_1,\Psi_2) = \tfrac{1}{2}c_1|\Psi_1|^4 + \tfrac{1}{2}c_2|\Psi_2|^4 + c_3|\Psi_1|^2|\Psi_2|^2 + b_1|\Psi_1|^2 + b_2|\Psi_2|^2 + a_0. \quad (20)$$

When Ψ_α are expressed in terms of ρ and $\vec{n}$ and the whole system is rescaled so that $m_\alpha \to 1$, we find

$$|\Psi_1|^2 = \rho^2(1+n_3), \quad |\Psi_2|^2 = \rho^2(1-n_3), \quad (21)$$

and then the potential [Eq. (20)] reads

$$V_0(\rho^2,n_3) = \rho^4\left\{n_3^2\left[\tfrac{1}{2}(c_1+c_2)-c_3\right] + n_3(c_1-c_2) + \tfrac{1}{2}(c_1+c_2) + c_3\right\} + \rho^2[n_3(b_1-b_2)+b_1+b_2] + a_0. \quad (22)$$

One important aspect in choosing the potential is that at infinity, the fields will settle to the minimum of the potential. Furthermore, in order to define the Hopf charge, it is necessary that the $\vec{n}$ field points to the same direction far away, otherwise we cannot compactify the three-dimensional (3D) space. It would therefore be optimal to have a potential with a minimum that would fix the $\vec{n}$ field completely, say, to $n_3=1$.

For a particular example, assume that $c := c_1 = c_2 = c_3 > 0$ and $b := b_1 = b_2$, then n_3 disappears from Eq. (22) and the potential minimum is at $\rho^2 = -b/(2c)$, $\vec{n}$ being free. For more generic parameter values, the extrema are obtained for particular values of n_3 and ρ^2,

$$n_3 = \frac{b_1(c_2+c_3) - b_2(c_1+c_3)}{b_1(c_2-c_3) + b_2(c_1-c_3)}, \quad (23)$$

$$\rho^2 = -\frac{b_1(c_2-c_3) + b_2(c_1-c_3)}{2(c_1c_2 - c_3^2)}. \quad (24)$$

This is a minimum, if $c_1c_2 > c_3^2$. Note that the above values do not necessarily fall within the allowed values for ρ^2 and n_3 (i.e., $\rho^2 > 0$ and $|n_3| \leq 1$), in which case the extrema are on the boundaries of the allowed values.

From physical arguments, the following special case is relevant:[29]

$$V_1(\Psi_1,\Psi_2) = \lambda((|\Psi_1|^2-1)^2 + (|\Psi_2|^2-1)^2). \quad (25)$$

This breaks $O(3)$ to $O(2)$ and corresponds to two independently conserved condensates. It has a minimum at $n_3=0$ and $\rho^2=1$.

Another physically relevant[29] potential is

$$V_2(\Psi_1,\Psi_2) = \lambda((|\Psi_1|^2-1)^2 + (|\Psi_2|^2-1)^2) + c|\Psi_1\Psi_2^* - \Psi_2\Psi_1^*| + a_0, \quad (26)$$

which breaks $O(3)$ completely. This corresponds to multiband superconductors with the interband Josephson effect.[29] In terms of $\vec{n}$, this potential is given [using Eq. (13)] as

$$V_2 = \lambda\tfrac{1}{2}n_3^2 + c\,\mathrm{Im}[(n_2 - in_1)e^{i2\alpha}] + b_0. \quad (27)$$

The minimum of this potential is located at $\rho^2 = 1/2$ and $n_3 = \sqrt{1-c^2/\lambda^2}$, while the specific values of n_1 and n_2 also depend on α, which is related to the phase of Ψ.

From the point of view of Hopf-charge conservation, the possibility of $\rho=0$ is problematic, even if it happens locally; since then, the field $\vec{n}$ is not defined. However, it has been argued[30] that quantum effects ensure that $\rho \neq 0$ everywhere. In classical field theories, like the present one, such expected quantum effects can be included through effective potentials. Since the main purpose of this effective potential is to guarantee that $\rho \neq 0$, its exact form is not so important. One such potential, which we will use later, is

$$V_{\mathrm{eff}}(\Psi_1,\Psi_2) = \tfrac{1}{4}\lambda(|\Psi_1|^2 + |\Psi_2|^2 - \rho_0^2)^2 + 2\gamma(|\Psi_1|^2 + |\Psi_2|^2)^{-1} + a_0. \quad (28)$$

The constants ρ_0 and a_0 are determined by requiring that the minimum of the potential is at $\rho^2=1$ with a value of 0, yielding $\rho_0^2 = 2 - \gamma/\lambda$ and $a_0 = -\gamma - \frac{\gamma^2}{4\lambda}$.

C. Initial states of Hopf invariant Q

We are interested in the minimum energy configurations of topologically distinct configurations of the field χ, or by Hopf map $\vec{n}$, related to the complex physical fields Ψ_α through Eqs. (2) and (13). From the point of view of $\vec{n}$, it is only necessary that $\lim_{|\vec{x}|\to\infty} \vec{n} = \vec{n}_\infty$ is the same in all directions. From this, it follows that we can compactify $\mathbb{R}^3 \to S^3$ and then $\vec{n}$ becomes a map $S^3 \to S^2$ with homotopy group $\pi_3(S^2) = \mathbb{Z}$, characterized by the Hopf charge.

Therefore, we have to create a configuration with $\Psi: \mathbb{R}^3 \to \mathbb{C}^2$ and $\vec{A}: \mathbb{R}^3 \to \mathbb{R}^3$, such that $\vec{n}$ has the desired property mentioned above. For Ψ_α, this implies $|\Psi_1|^2 + |\Psi_2|^2 \neq 0$ everywhere and $\lim_{|\vec{x}|\to\infty} \Psi_\alpha$ are (independent) constants. The first condition is also necessary for defining the field χ and if the second condition is also satisfied, χ becomes a map $S^3 \to S^3$.

The method of constructing a configuration with a desired Hopf charge has been investigated by Aratyn *et al.*[31] They used the fact that for any function $\phi: S^3 \to S^3$ combined with the Hopf map $h: S^3 \to S^2$,

$$h(\phi_1,\phi_2,\phi_3,\phi_4) = \begin{pmatrix} 2(\phi_1\phi_3 - \phi_2\phi_4) \\ -2(\phi_1\phi_4 + \phi_2\phi_3) \\ \phi_1^2 + \phi_2^2 - \phi_3^2 - \phi_4^2 \end{pmatrix}, \quad (29)$$

the Hopf charge of $h \circ \phi: S^3 \to S^2$ equals the degree of the map $\phi: S^3 \to S^3$ (the degree is the n-dimensional generalization of the one-dimensional degree, also known as the winding number).

For an explicit construction, one uses the toroidal coordinates (η, ξ, φ) of $\mathbb{R}^3$ defined by

$$x_1 = \frac{\sinh(\eta)\cos(\varphi)}{\Delta}, \quad x_2 = \frac{\sinh(\eta)\sin(\varphi)}{\Delta},$$

$$x_3 = \frac{\sin(\xi)}{\Delta}, \quad \Delta = \cosh(\eta) - \cos(\xi). \quad (30)$$

In these coordinates, the core is at $\eta=\infty$, while the z axis and spatial infinity are at $\eta=0$.

Next, take any monotonic function $g: [0,\infty) \to [0,1]$, (or $[-1,0]$), choose $p,q \in \mathbb{Z}$, and define the map $\phi: S^3 \to S^3$ by

$$\phi = \big(g(\eta)\cos(p\xi), g(\eta)\sin(p\xi), \sqrt{1-g(\eta)^2}\cos(q\varphi), \sqrt{1-g(\eta)^2}\sin(q\varphi)\big). \quad (31)$$

If, furthermore, g is such that $g^2(\infty)-g^2(0)=\pm 1$, then the combined map, $h\circ\phi$, has the Hopf invariant,

$$H(h\circ\phi) = \pm pq. \quad (32)$$

For details, see Ref. 31. Using Eq. (31), we now identify

$$\chi_1 := \phi_1 + i\phi_2 = g(\eta)e^{ip\xi}, \quad (33a)$$

$$\chi_2 := \phi_3 + i\phi_4 = \sqrt{1-g(\eta)^2}e^{iq\varphi}. \quad (33b)$$

At the z axis, χ_2 looks like a φ vortex, and therefore for continuity, we add the further requirement that $g(0)=\pm 1$. Similarly, around the core (located at $\eta=\infty$), we have a ξ vortex, and therefore we demand that $g(\infty)=0$.

From Eqs. (12) and (33), we obtain

$$\vec{n}(\vec{x}) = \begin{pmatrix} 2g(\eta)\sqrt{1-g^2}\cos(p\xi+q\varphi) \\ -2g(\eta)\sqrt{1-g^2}\sin(p\xi+q\varphi) \\ 2g^2(\eta)-1 \end{pmatrix}. \quad (34)$$

Finally, to close the loop, the χ of the Eq. (33) can be recovered from Eq. (13) using Eq. (34) and choosing $\alpha=-q\varphi$. Note that since $\eta=0$ at infinity and $g(0)^2=1$, the above construction implies $\vec{n}_\infty := \lim_{|\vec{x}|\to\infty}\vec{n}=(0,0,1)$.

Inverting the toroidal coordinates defined in Eq. (30) enables us to express Eq. (33) in the Cartesian coordinates. In addition, denoting $r^2=x_1^2+x_2^2+x_3^2$ and choosing $\rho=1$, $g(\eta)=1/\cosh(\eta)$, we obtain

$$\Psi_1(\vec{x}) = \frac{\sqrt{(r^2-1)^2+4x_3^2}}{r^2+1}\left(\frac{r^2-1-2ix_3}{\sqrt{(r^2-1)^2+4x_3^2}}\right)^p, \quad (35a)$$

$$\Psi_2(\vec{x}) = \frac{2\sqrt{x_1^2+x_2^2}}{r^2+1}\left(\frac{x_1+ix_2}{\sqrt{x_1^2+x_2^2}}\right)^q. \quad (35b)$$

This is the formula used for the initial configurations of Ψ_α for our numerical computations. The state indeed has the correct Hopf invariant, which, in the case of $p=q=1$, can be seen by finding the preimages of $\Psi_\alpha=0$, which correspond to preimages of $n_3=\pm 1$. These form two closed loops, namely, $r=1, x_3=0$ for $\Psi_1=0$ and the z axis, which in the compactified space S^3 is actually closed.

Fixing $\vec{n}$ or χ_i does not say anything about the magnitude of Ψ. From energy consideration, we must choose $\lim_{|\vec{x}|\to\infty}\Psi_\alpha$ to be one of the minima of the potential and this fixes a *preferred* value for ρ. We use this preferred value for all $\vec{x}$ when constructing the initial configurations.

III. NUMERICS

In this section, we will describe the discretization of the model and the method of the minimization of the Lagrangian (1). We will also compare the GL to FS model and present some test calculations and the parameters as well as coupling constants for the simulations.

It is important to note that all our simulations are done with the fields Ψ_α only; the fields $\vec{n}$, ρ, and $\vec{C}$ are never used in any computation, they are only used in the analysis of the results. It is perhaps useful to mention once again that the change of variables in Eqs. (2)–(4) is not reversible whenever $\rho(\vec{x})=0$. There is, however, no guarantee that ρ stays nonzero in numerical simulations of the physical fields Ψ_α and $\vec{A}$, even if the minimum of the potential is at a nonzero value of ρ. The situation when $\rho=0$ locally can imply breakdown in topology, and therefore in our numerical simulations, we have monitored the changes in the global minimum value of ρ.

Topology can also break if the topological structure shrinks smaller than the lattice unit length. In order to be aware of this possibility, we have monitored the global minimum of the dot product of nearest-neighbor $\vec{n}$-vectors: when the global minimum becomes negative, the lattice is probably too coarse, or the configuration has a genuine singularity. When this has happened in the simulations, we have repeated the simulation with ever increasing lattice size until the computing resources were exhausted. This strongly points to a singular configuration.

For simplicity, we have used the rescaled $(|\Psi_\alpha|^2/m_\alpha \to |\Psi_\alpha|^2)$ Lagrangian and natural units ($c=\hbar=1$) throughout our numerical work. With these choices, the Lagrangian density used in all our numerical simulations becomes

$$\mathcal{L} = \tfrac{1}{2}|(\nabla + ig\vec{A})\Psi_1|^2 + \tfrac{1}{2}|(\nabla - ig\vec{A})\Psi_2|^2 + \tfrac{1}{2}g_f(\nabla\times\vec{A})^2 + V(\Psi_{1,2}). \quad (36)$$

This can be further scaled by $\vec{A}\to\frac{1}{g}\vec{A}$, which reveals the fact that the only relevant parameter is $g^2/g_f=4\mu_0 e^2$. The values used in numerical simulations are $g=1$ and $g_f \in \{0.01, 1, 2, 100\}$; these amount to a particular choice of units for μ_0 and e.

In our studies of the FS model, we have always assumed that $\lim_{|x|\to\infty} n_3=1$, but some of the present potentials, e.g., V_1, do not have that as a minimum. In this case, we may assume that $\lim_{|x|\to\infty} n_2=1$, but this can be transformed to $n_3=1$ by a global rotation in the configuration space, which takes $n_3\to n_2$ and $n_2\to -n_3$. The same effect can be achieved by using new fields defined by

$$\Psi_1' = \frac{1}{\sqrt{2}}(\Psi_1 + i\Psi_2^*), \quad \Psi_2' = \frac{1}{\sqrt{2}}(\Psi_1 - i\Psi_2^*), \quad (37)$$

changing V_1 of Eq. (25) to

$$V_{1_{\rm rot}} = \lambda[(|\Psi_1|^2+|\Psi_2|^2-2)^2 - (\Psi_1\Psi_2 - \Psi_1^*\Psi_2^*)^2]. \quad (38)$$

The different potential terms also contain various parameters. For V_0, we have always used $4c_1=4c_2=2c_3=-b_1=-b_2=a_0$, which, denoting $\lambda\equiv\frac{1}{2}c_1$, enables us to write $V_0=\lambda(|\Psi_1|^2+|\Psi_2|^2-2)^2$. In the numerical simulations, we have used potentials V_0, $V_{1_{\rm rot}}$, and $V_{\rm eff}$ with $\lambda \in \{0, 1, 4, 100, 1000\}$.

A. Discretization

The system has been discretized on a cubic rectangular lattice [indexed as (s,u,v)] with periodic boundary conditions. Our model can be considered as a two-component version of the time-independent, ordinary Abelian $\mathbb{U}(1)$ Higgs model, which has long since been discretized for lattice simulations in quantum field theory (for example, see Refs. 32 and 33 and the references therein). The main point in that context is to discretize the fields so that gauge invariance is preserved. From Eq. (6), we see that if we use the forward discretization of the derivatives, the gauge transformation of A_k has to be discretized as follows:

$$A_{1|s,u,v} \to A_{1|s,u,v} + \frac{c}{a}(\theta_{s+1,u,v} - \theta_{s,u,v}), \tag{39a}$$

$$A_{2|s,u,v} \to A_{2|s,u,v} + \frac{c}{a}(\theta_{s,u+1,v} - \theta_{s,u,v}), \tag{39b}$$

$$A_{3|s,u,v} \to A_{3|s,u,v} + \frac{c}{a}(\theta_{s,u,v+1} - \theta_{s,u,v}), \tag{39c}$$

where a is the lattice parameter. Thus, A_k should be considered as living on the link between two lattice points parallel to the coordinate axis k. Combining this discretization with the way the Ψ_α transforms in Eq. (6), it follows that the following combination,

$$\Psi^*_{1|s+1,u,v}\Psi_{1|s,u,v}e^{-ia\kappa A_{1|s,u,v}} + \Psi_{1|s+1,u,v}\Psi^*_{1|s,u,v}e^{ia\kappa A_{1|s,u,v}} - \Psi^*_{1|s+1,u,v}\Psi_{1|s+1,u,v} - \Psi^*_{1|s,u,v}\Psi_{1|s,u,v}, \tag{40}$$

where $\kappa=\frac{2e}{\hbar c}$, is gauge invariant. If we calculate its continuum limit as $a\to 0$ by expanding in a [e.g., $\Psi_{1|s+1,u,v} = \Psi_1(x+a,y,z) = \Psi_1(x,y,z) + a\partial_x\Psi_1(x,y,z) + \frac{1}{2}a^2\partial_x^2\Psi_1(x,y,z) + \cdots$], we obtain $-a^2|(\partial_1 + i\kappa A_1)\Psi_1|^2 + O(a^3)$. For Ψ_2 with A_1, we use a similar expression with $\kappa\to-\kappa$. Finally, for the other components of $\vec{A}$, we use corresponding shifts, as illustrated in Eqs. (39) and (40).

For the discretization of $\vec{B}^2$, we use the expression

$$e^{iF_{12|suv}} + e^{-iF_{12|suv}} + e^{iF_{23|suv}} + e^{-iF_{23|suv}} + e^{iF_{31|suv}} + e^{-iF_{31|suv}} - 6, \tag{41}$$

where, for example,

$$F_{12|suv} = A_{1,s,u+1,v} - A_{1,s,u,v} - A_{2,s+1,u,v} + A_{2,s,u,v}. \tag{42}$$

The F_{kl} are gauge invariant under Eq. (39), and the continuum limit of Eq. (41) with Eq. (42) is $-a^2(\nabla\times\vec{A})^2 + O(a^3)$.

For the potential, we use $a^2V(\Psi_{\alpha|suv})$. The discretized Lagrangian is the sum of all the above terms multiplied by $-a/2$, and then the resulting sum has the continuum limit of Eq. (36). In practice, we use the cubic lattices of sizes of $60^3,\ldots,960^3$. Of these, just the sizes 240^3, 480^3, and 720^3 are used in actual simulations, the remaining sizes used only to verify the code, results, and discretization.

The minimization of the Lagrangian has been done using the steepest descent method and the Fletcher-Reeves variant of the conjugate gradient method. The gradients needed have been calculated symbolically from the discretized Lagrangian.

B. Initial states

In order to start the simulations, we have to generate initial states with specified Hopf invariants. These initial configurations have been made using Eq. (35) and choosing ρ such that $V(\Psi_\infty)=0$. Three different values of Hopf invariant were used: 1, 2, and 4. However, this leaves $\vec{A}$ undetermined. The topology of the system is unaffected by $\vec{A}$, so, in principle, we can choose any configuration for it. We have used several different initial configurations for $\vec{A}$; for all the results presented here, we have used two choices. The first one is defined by the condition $\vec{C}=0\Rightarrow\vec{A}=\frac{\hbar c}{4e}\vec{j}$ by Eqs. (10) and (11). This choice enables us to test the validity of the program by comparing the energies of the initial states with those obtained for the pure FS model. The second initial configuration has been constructed by solving Ampère's law for $\vec{A}$ with fixed Ψ_α. Note that since we use gradient methods to minimize the energy, we already have encoded Ampère's law in our program: the gradients of the Lagrangian with respect to A_k indeed yield Ampère's law.

As a further test of discretization, we used the same initial configurations in lattices of different sizes and with different lattice constants. With lattice sizes of 240^3 and above, the energies were within 1% of each other.

C. Comparison with previous Faddeev-Skyrme studies

We have also compared the new calculations with those presented in Ref. 13. By using an initial configuration, where $\rho\equiv 1$, $\vec{C}\equiv 0$, and $V\equiv 0$, the GL model [Eq. (19)] reduces to the FS model [Eq. (14). In particular, the magnetic term becomes $E_{M_B}=\frac{\hbar^2}{128\mu_0 e^2}[\epsilon_{klm}(\vec{n}\cdot\partial_l\vec{n}\times\partial_m\vec{n})]^2$, while in the FS model, we have $E_{T_{FS}}=\frac{1}{2}g_{FS}(\vec{n}\cdot\partial_k\vec{n}\times\partial_l\vec{n})^2$. If we set $c=\hbar=1$, $e=\frac{1}{2}$, $\mu_0=1$, and $g_{FS}=\frac{1}{8}$ (the value most commonly used in our earlier work), we have $E_{T_{FS}}=2E_{M_B}$. We created the same initial configuration with our old and new codes and found that the energies of the initial states agree to within 1% with a lattice of 120^3.

During the calculations, we have monitored the topology of the system. As we saw in Sec. II B, the conservation of topology is not guaranteed whenever $\rho\to 0$. Therefore, we have followed the value of the global minimum of ρ^2. In keeping with our earlier work, we have also monitored the dot products of $\vec{n}(\vec{x})\cdot\vec{n}(\vec{x}+\vec{\mu})$, [where $\vec{\mu}\in\{(1,0,0),(0,1,0),(0,0,1)\}$]. When the global minimum of this dot product approaches zero or becomes even negative, it indicates possible breakdown of continuity and therefore of topology during the simulation.

We have also calculated the value of the Hopf invariant directly from the field configuration. Using the basic differential geometric result of $H(h\circ\chi\equiv\vec{n})=\deg\chi$, we can even use our computational field variables. Since for any map $f\in C^\infty(S^3,S^3)$,

$$\deg f = \frac{1}{2 \cdot 3! \pi^2} \int_{S^3} \epsilon_{\mu\nu\sigma\rho} f^\mu df^\nu \wedge df^\sigma \wedge df^\rho, \qquad (43)$$

we can compute the value of the Hopf invariant by numerical integration. The Hopf invariant can also be determined by visual inspection of the linking numbers of the preimages.

IV. RESULTS AND DISCUSSION

A necessary condition for any stable static localized structure is its stability against scaling. Let us assume, for now, that $\rho \neq 0$ everywhere. Then, the simple scaling argument of Derrick[34] gives a necessary condition for the stability against scaling. Consider the behavior of the energy under scaling $x \to \lambda x$. For the FS model in 3D, the volume element of the energy integral behaves like λ^3, while in the integrand [Eq. (14)] the first term scales as λ^{-2} and the second one as λ^{-4}. In the integral, the two terms then have opposite scaling behavior and if each is positive definite, one cannot scale the energy to zero. Furthermore, by the virial theorem, the preferred scaling is the one where the two terms have equal value. In fact, one can show[35] that in the FS model, the energy is bounded from below by the Hopf charge: $E > c|Q|^{3/4}$. This has also been confirmed numerically.[10–13]

In the present model, the scaling stability hinges on the behavior of the first and last terms in Eq. (19). These terms are positive definite and their scaling properties are opposite and thus, as long as they are both nonzero, the system is stable. The last term, however, equals the term $\vec{B}^2$ in Eq. (1) and could, in principle, vanish. Indeed, if the $\vec{C}$ field obtained such a value that

$$\epsilon_{klm} \partial_l C_m = -\epsilon_{klm} \vec{n} \cdot \partial_l \vec{n} \times \partial_m \vec{n}, \qquad (44)$$

then the last term would vanish, rendering the system unstable against scaling. One could say that topological charge leaks from $\vec{n}$ to $\vec{C}$, so that $\vec{B} \to 0$.

We have observed the above scaling instability in direct minimizations of all fields. The minimization does not exactly follow the route of a uniform scaling, but we have observed that the toruslike unknot shrinks into a thin tube, and the value of the integrand in Eq. (43), which contributes to the topological charge, concentrates tightly in a region near the vortex core. Eventually, the nearest-neighbor values in the corresponding $\vec{n}$ are antiparallel, which, in effect, means that the vortex configuration has shrunk to a size less than the lattice spacing. This is accompanied with ρ approaching zero, and we have verified that ρ approaches zero at the same location where the neighboring $\vec{n}$ are antiparallel. At a place where $\rho=0$, the field $\vec{n}$ can no longer be determined from Ψ, and the topological structure breaks, after which the system rapidly goes to a vacuum state. We have observed this scenario for various different potential forms and strengths.

Two steps of the process of topology breakdown are illustrated in Fig. 1, where we have plotted two distinct preimages of $\vec{n}$, $n_2=1$ and $n_2=-1$, and the isosurface, $n_3=0$, on which the tubes lie; the colors (grayscale) of the isosurface describe longitudes. Initially, (left image) the preimages are spaced 90° apart on the isosurface $n_3=0$, but during the minimization, on the region of xy plane inside the torus core, the preimages deform so that eventually there are no lattice points between the preimages of $n_2=1$ and $n_2=-1$. This happens even with V_{eff} (in which case $\rho>0$ everywhere) and is not accompanied by a shrinking torus; the torus deforms somewhat but the radius of the inner intersection of $n_3=0$ and xy plane stays approximately constant. The two preimages eventually touch each other and when they drift apart again (right image), they have become reconnected so that the topology is trivial. After this, there is nothing to prevent the energy from dropping to zero.

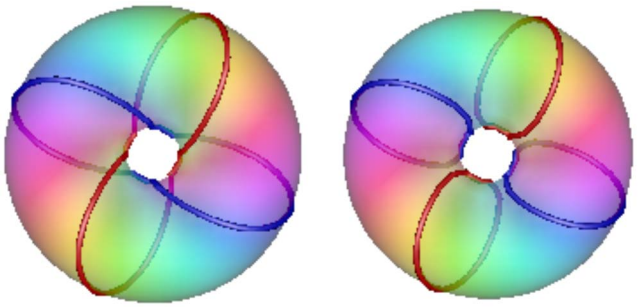

FIG. 1. (Color online) Snapshots of the preimages in the relaxation of the $(p,q)=(1,2)$ unknot, before (left) and just after (right) topology breakdown. The tubes correspond to the preimages of $n_2 = \pm 1$. The coloring on the $n_3=0$ isosurface corresponds to the longitude of $\vec{n}$.

It should be noted, however, that for any nontrivial configuration Ψ_α, Eq. (44) violates Ampère's law [Eq. (8)] because by using Eqs. (18), (17), and (8), Eq. (44) implies $\vec{B}=0$ and $\nabla \times \vec{B} = \vec{J} = 0$, which contradicts the topological nontriviality of Ψ_α. Thus, any nontrivial configuration, where Eq. (44) holds, is unphysical. It can then be argued that although the scaling route leads to instability, it does so via nonphysical states and thus does not imply the instability of physically relevant states.

In order to stay within physically relevant states during minimization, we have used the following procedure. After every minimization step applied to the Ψ fields, we check whether Ampère's law [Eq. (8)] is satisfied. At the beginning of a simulation, the Ψ fields are generated from analytical formulas, such as Eq. (35), which provide the proper topological charge. Then, Ampère's law is solved for this initial state (using conjugate gradients) until is it "sufficiently accurate." After this initial step, we take conjugate gradient iteration steps for all fields until the convergence criterion for $\vec{A}$ is no longer satisfied, at which point we continue only with $\vec{A}$ and Ampère's law until it is satisfied to the desired accuracy. This is repeated until the whole iteration has converged. There are various methods to determine when the solution is sufficiently accurate. Since we use a gradient-based method to solve Ampère's law, it is natural to determine the accuracy of the solution using the gradients. To accomplish this, we observe the absolute values of the gradients affecting $\vec{A}$ and note the maximum of these values at each iteration and the initial state before any iterations are made. We then compare

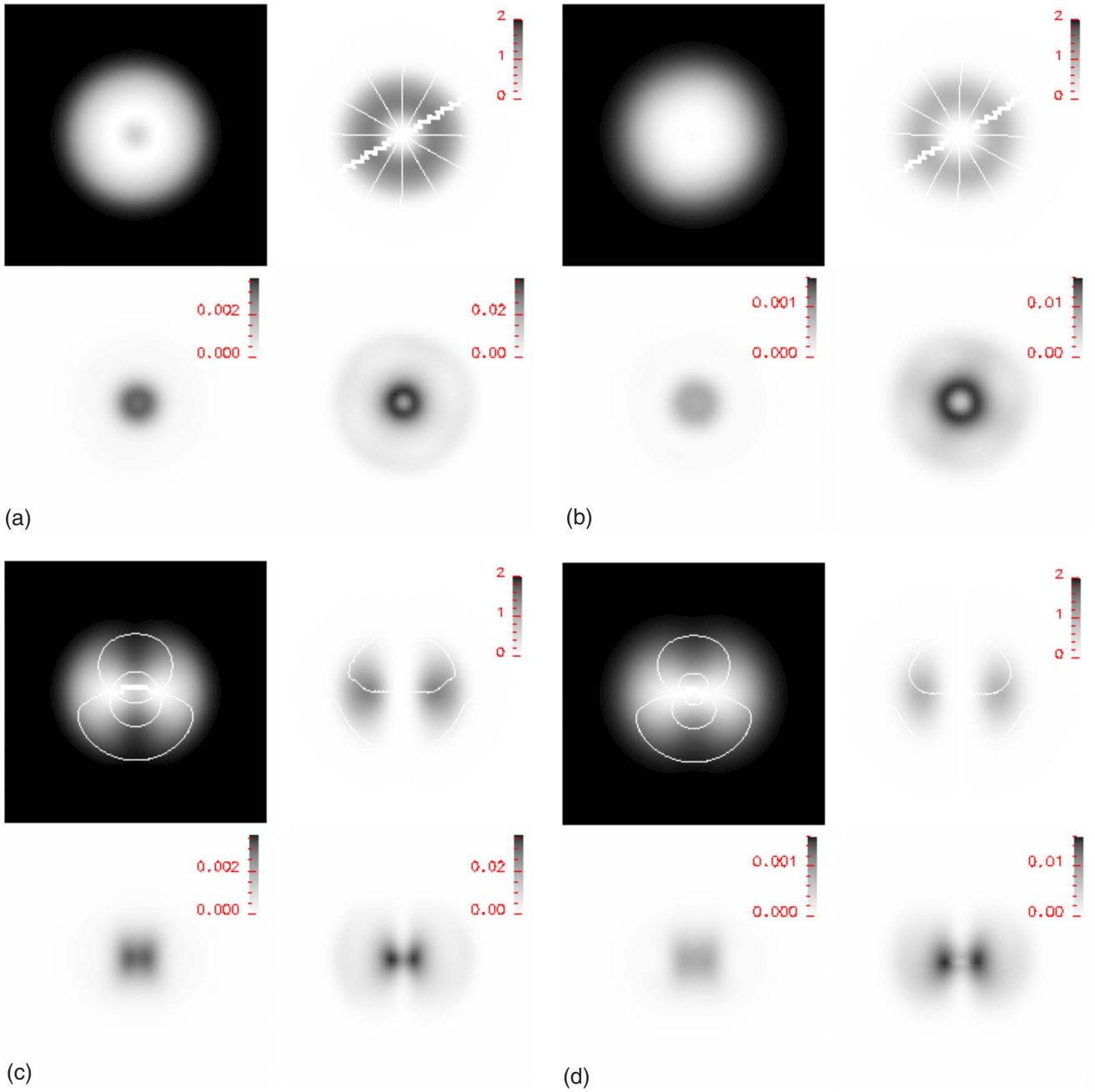

FIG. 2. (Color online) Snapshots of a $Q=2$ system [(a) and (c)] before and [(b) and (d)] just after the topology breakdown. Cross sections of the system have been taken in [(a) and (b)] xy plane and [(c) and (d)] xz plane. In all four panels, the upper two plots describe the densities $|\Psi_1|^2$ (left) and $|\Psi_2|^2$ (right) on which the phases of the condensates are superimposed as contours spaced $\pi/3$ apart; the lower two plots of each panel describe the energy densities $\frac{1}{2}g_f|\vec{B}|^2$ (left) and $E_{\text{tot}}-\frac{1}{2}g_f|\vec{B}|^2$ (right). The jagged line in the xy cross sections corresponds to $\phi=\pi$; the jaggedness itself is an imaging artifact caused by the discreteness of the data used to produce the image.

these maxima with the maximum found at the initial state; the solution is considered sufficiently accurate if the ratio of the current maximum to the initial maximum is below 0.0001.

The result of the minimization process is always the same: a singular configuration of Ψ_α, where the region contributing to the topological charge has shrunk to a singular line. At the same time, $\vec{B}$ field is generated in the hole of the torus. This can be seen from Fig. 2, which describes states before and just after topology breakdown. In particular, one can see how the $\vec{B}$ is formed mostly on a smaller ring in the torus hole and how the initial maximum of Ψ_1 at origin vanishes while its toroidal minimum becomes disk shaped. The topology is broken in exactly the same way as in the unconstrained case.

The exact type of singularity and the process which leads to its formation depends on the potential. For V_0 and V_{eff}, the small radius of any initial torus-type isosurface of n_3 shrinks without limit, snaring the region of topological interest into a singular loop. For $V_{1_{\text{rot}}}$, the process is the same unless the

potential is very strong, in which case the region, where $n_2 \neq 0$, shrinks to a surface.

This process is ultimately a scaling instability, albeit a different one from the one considered at the beginning of this section. Now, the scaling is not global but only shrink the smaller circle of the torus. The terms involving derivatives of Ψ_α grow without limit during the shrinking process, but only on a loop or a surface, allowing still the total energy to decrease.

In every case, the shrinking continues until the discreteness of the computational lattice eventually breaks the topology. We have tried to follow the development of this singularity by increasing lattice density. In each case, a singularity is reached, but, in principle, the shrinking can stop at some still smaller scale determined by the dimensional parameters of the system (such as penetration length, strength of the potential, etc.).

V. CONCLUSIONS

We have investigated numerically the two-component Ginzburg-Landau model using as initial states torus unknots, with nonvanishing Hopf change Q; this brings a topological structure into the system. We have used different types of potentials depending on both order parameters Ψ_α of the system. In all cases, the initial torus tube shrinks into a thin loop and becomes untrackable in our computational discrete lattice: the discreteness allows the topological structure of the system to disappear eventually, contrary to the case of the Faddeev-Skyrme model. The topological stability in the FS model is due to the fact that the kinetic and topological terms are nonvanishing and have an opposite behavior in the scaling. In the GL model, the term corresponding to the FS topological term is the magnetic field term which contributes to the unstability of the system. In a direct minimization of the fields, the topological charge leaks from $\vec{n}$ into $\vec{C}$ allowing eventually the Derrick-type instability, while in minimizations respecting Ampère's law, the process is milder, but nevertheless leads to singularity.

Thus, it seems that the two-component GL model does not support stable topological structures having a nontrivial conserved Hopf invariant due to this scaling instability. It is still possible that in the GL system, the natural size of a stable unknot is much smaller than in the FS model or that it is only stable for suitably strong potentials. It is also possible to stabilize the topological structures by adding a suitable term in the Lagrangian. One such term has been introduced in Ref. 36. These are questions that we will study further.

ACKNOWLEDGMENTS

We greatly acknowledge generous computing resources from the M-grid project, supported by the Academy of Finland, and from CSC—Scientific Computing Ltd., Espoo, Finland. This work has partly been supported by the Academy of Finland through its Center of Excellence program. One of us (J.J.) also wishes to thank the Jenny and Antti Wihuri Foundation for a supporting grant.

*juolja@utu.fi
†hietarin@utu.fi
‡Petri.Salo@tkk.fi

[1] J. R. Abo-Shaeer, C. Raman, J. M. Vogels, and W. Ketterle, Science **292**, 476 (2001).
[2] P. Engels, I. Coddington, P. C. Haljan, V. Schweikhard, and E. A. Cornell, Phys. Rev. Lett. **90**, 170405 (2003).
[3] R. Monaco, J. Mygind, M. Aaroe, R. J. Rivers, and V. P. Koshelets, Phys. Rev. Lett. **96**, 180604 (2006).
[4] R. Monaco, J. Mygind, and R. J. Rivers, Phys. Rev. Lett. **89**, 080603 (2002).
[5] R. Carmi, E. Polturak, and G. Koren, Phys. Rev. Lett. **84**, 4966 (2000).
[6] Ü. Parts, J. M. Karimäki, J. H. Koivuniemi, M. Krusius, V. M. H. Ruutu, E. V. Thuneberg, and G. E. Volovik, Phys. Rev. Lett. **75**, 3320 (1995).
[7] A. P. Finne, S. Boldarev, V. B. Eltsov, and M. Krusius, J. Low Temp. Phys. **136**, 249 (2004).
[8] R. Ray and A. M. Srivastava, Phys. Rev. D **69**, 103525 (2004).
[9] L. D. Faddeev and A. J. Niemi, Nature (London) **387**, 58 (1997).
[10] R. A. Battye and P. M. Sutcliffe, Phys. Rev. Lett. **81**, 4798 (1998).
[11] R. A. Battye and P. Sutcliffe, Proc. R. Soc. London, Ser. A **455**, 4305 (1999).
[12] J. Hietarinta and P. Salo, Phys. Lett. B **451**, 60 (1999).
[13] J. Hietarinta and P. Salo, Phys. Rev. D **62**, 081701(R) (2000).
[14] J. Hietarinta, J. Jäykkä, and P. Salo, Phys. Lett. A **321**, 324 (2004).
[15] C. Adam, J. Sanchez-Guillen, and A. Wereszczynski, Eur. Phys. J. C **47**, 513 (2006).
[16] J. P. Martikainen, A. Collin, and K. A. Suominen, Phys. Rev. Lett. **88**, 090404 (2002).
[17] M. Mackie, O. Dannenberg, J. Piilo, K.-A. Suominen, and J. Javanainen, Phys. Rev. A **69**, 053614 (2004).
[18] J. Ruostekoski and Z. Dutton, Phys. Rev. A **72**, 063626 (2005).
[19] X.-J. Liu, H. Jing, X. Liu, and M.-L. Ge, Eur. Phys. J. D **37**, 261 (2006).
[20] E. Smorgrav, J. Smiseth, E. Babaev, and A. Sudbo, Phys. Rev. Lett. **94**, 096401 (2005).
[21] M. Donaire, T. W. B. Kibble, and A. Rajantie, New J. Phys. **9**, 148 (2007).
[22] V. B. Eltsov, A. P. Finne, R. Hanninen, J. Kopu, M. Krusius, M. Tsubota, and E. V. Thuneberg, Phys. Rev. Lett. **96**, 215302 (2006).
[23] A. P. Finne, T. Araki, R. Blaauwgeers, V. B. Eltsov, N. B. Kopnin, M. Krusius, L. Skrbek, M. Tsubota, and G. E. Volovik, Nature (London) **424**, 1022 (2003).
[24] E. Babaev, A. Sudbo, and N. W. Ashcroft, Nature (London) **431**, 666 (2004).
[25] E. Babaev, Phys. Rev. D **70**, 043001 (2004).
[26] L. D. Faddeev, Lett. Math. Phys. **1**, 289 (1976).
[27] E. Babaev, L. D. Faddeev, and A. J. Niemi, Phys. Rev. B **65**,

100512(R) (2002).
[28] There seems to be contradiction in the sign of j_k between what we obtain here and what is obtained after Eq. (4) in Ref. 27. This affects some signs of other formulas as well.
[29] E. Babaev (private communication).
[30] L. Faddeev and A. J. Niemi, Phys. Rev. Lett. **85**, 3416 (2000).
[31] H. Aratyn, L. A. Ferreira, and A. H. Zimerman, Phys. Rev. Lett. **83**, 1723 (1999).
[32] K. G. Wilson, Phys. Rev. D **10**, 2445 (1974).
[33] P. H. Damgaard and U. M. Heller, Phys. Rev. Lett. **60**, 1246 (1988).
[34] G. H. Derrick, J. Math. Phys. **5**, 1252 (1964).
[35] A. F. Vakulenko and L. V. Kapitanskii, Sov. Phys. Dokl. **24**, 433 (1979).
[36] R. S. Ward, Phys. Rev. D **66**, 041701(R) (2002).